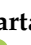


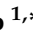



Article

UiO-66 MOF-Derived Ru@ZrO₂ Catalysts for Photo-Thermal CO₂ Hydrogenation

Fernando Almazán¹, Marta Lafuente², Amaya Echarte¹, Mikel Imizcoz¹, Ismael Pellejero^{1,*}
and Luis M. Gandía^{1,*}

¹ Institute for Advanced Materials and Mathematics (InaMat2), Universidad Pública de Navarra (UPNA), Campus de Arrosadia, 31006 Pamplona-Iruña, Spain; fernando.almazan@unavarra.es (F.A.); amaya.echarte@unavarra.es (A.E.); mikel.imizcoz@unavarra.es (M.I.)

² Universidad de Zaragoza (UNIZAR), Campus San Francisco, 50014 Zaragoza, Spain; martalaf@unizar.es

* Correspondence: ismael.pellejero@unavarra.es (I.P.); lgandia@unavarra.es (L.M.G.)

Abstract: The use of metal–organic frameworks (MOFs) as templates or precursors in the manufacture of heterogeneous catalysts is highly attractive due to the transfer of MOFs' inherent porosity and homogeneous metallic distribution to the derived structure. Herein, we report on the preparation of MOF-derived Ru@ZrO₂ catalysts by controlled thermal treatment of zirconium-based MOF UiO-66 with ruthenium moieties. Ru³⁺ (3 or 10 mol%) precursor was added to UiO-66 synthesis and, subsequently, the as-synthesized hybrid structure was calcined in flowing air at different temperatures (400–600 °C) to obtain ZrO₂-derived oxides doped with highly dispersed Ru metallic clusters. The materials were tested for the catalytic photo-thermal conversion of CO₂ to CH₄. Methanation experiments were conducted in a continuous flow (feed flow rate of 5 sccm and 1:4 CO₂ to H₂ molar ratio) reactor at temperatures from 80 to 300 °C. Ru_{0.10}@ZrO₂ catalyst calcined at 600 °C was able to hydrogenate CO₂ to CH₄ with production rates up to 65 mmol_{CH₄}·g_{cat.}⁻¹·h⁻¹, CH₄ yield of 80% and nearly 100% selectivity at 300 °C. The effect of the illumination was investigated with this catalyst using a high-power visible LED. A CO₂ conversion enhancement from 18% to 38% was measured when 24 sun of visible LED radiation was applied, mainly due to the increase in the temperature as a result of the efficient absorption of the radiation received. MOF-derived Ru@ZrO₂ catalysts have resulted to be noticeably active materials for the photo-thermal hydrogenation of CO₂ for the purpose of the production of carbon-neutral methane. A remarkable effect of the ZrO₂ crystalline phase on the CH₄ selectivity has been found, with monoclinic zirconia being much more selective to CH₄ than its cubic allotrope.

Keywords: MOF-derived catalyst; UiO-66; photo-thermal catalysis; CO₂ hydrogenation; carbon neutral fuels; zirconia; calcination



Citation: Almazán, F.; Lafuente, M.; Echarte, A.; Imizcoz, M.; Pellejero, I.; Gandía, L.M. UiO-66 MOF-Derived Ru@ZrO₂ Catalysts for Photo-Thermal CO₂ Hydrogenation. *Chemistry* **2023**, *5*, 720–729. <https://doi.org/10.3390/chemistry5020051>

Academic Editor: Tomas Ramirez Reina

Received: 2 March 2023

Revised: 20 March 2023

Accepted: 23 March 2023

Published: 25 March 2023



Copyright: © 2023 by the authors. Licensee MDPI, Basel, Switzerland. This article is an open access article distributed under the terms and conditions of the Creative Commons Attribution (CC BY) license (<https://creativecommons.org/licenses/by/4.0/>).

1. Introduction

Anthropogenic emission of greenhouse gases is causing an extraordinary increment of atmospheric CO₂ levels, leading to the rise of global temperature in a very short period of time [1]. During the last two decades, enormous efforts have been carried out for decarbonizing transportation and industrial processes in order to mitigate carbon dioxide emissions, so the development of technologies able of recycling CO₂ into value-added products is highly desired [2–5]. Carbon-neutral fuels obtained from CO₂ directly captured from air or other sources, such as biomass or organic wastes, is considered a very promising way of mitigating overall carbon emissions, while at the same time, taking advantage of the use of existing infrastructures and technologies [6]. For this purpose, one of the most interesting processes for recycling anthropogenic CO₂ is the Sabatier reaction, first reported in 1902 [7,8], which consists of the exothermic hydrogenation of carbon dioxide to produce methane and water.

Photo-thermal catalysis is the synergistic combination of photo- and thermochemical processes that occur under broad solar spectrum illumination of the catalyst, resulting in the promotion of the chemical reaction [9–12]. The photo-thermal effect holds promising features for the valorization of CO₂ into solar fuels using green hydrogen as a chemical vector and solar light as the sole energy input [13,14]. The photo-thermal CO₂ methanation can be conducted under light using noble metals nanoparticles (NPs) based mainly on Pd, Rh and Ru as active catalysts, though the more abundant and less costly transition metals such Ni or Co [11,15–18] can be also used. The good performance of the catalytic system depends not only on the properties of the metallic nanoparticle, but also on the physical and chemical characteristics of the support (large light absorption band, high surface area, thermal conductivity, etc.) that plays key roles in the CO₂ adsorption and activation processes. The distribution and size of the metallic nanoparticles on the support and the interface between them are also crucial for proper activity and selectivity [19–22]. Looking for these convenient properties, in recent years, the use of metal–organic frameworks (MOFs) as templates or precursors for the manufacture of heterogeneous catalysts has gained attention due to the MOFs' inherent porosity and homogeneous metallic distribution, which is also transferred to the derived structure [23–25]. MOFs-derived materials can be obtained upon thermal treatment under inert gas atmosphere to produce carbonaceous solids [26], or under oxidizing atmospheres to obtain metallic oxides [27–29]. In both cases, the selection of the conditions, i.e., temperature and time of the thermal treatment, is crucial to obtain active materials. It is necessary to guarantee the complete degradation/removal of the parent organic ligands while avoiding large particle growth to minimize aggregation and loss of surface area.

Herein, we present the synthesis of a CO₂ methanation catalyst from a well known Zr(IV)-based MOF UiO-66 (Zr-BDC (Benzene-1,4-dicarboxylic acid)) [30] through the addition of controlled amounts of Ru³⁺. It is possible in this way to keep the MOF porous structure while containing the active metal fully dispersed within the framework [31,32]. The incorporation of addenda atoms to a stable MOF structure provokes defects in the crystalline network, resulting in unstable structures [33]. Subsequent controlled calcination yields zirconium oxide doped with highly dispersed Ru clusters. To achieve this non-trivial target (high metal dispersion and controlled support properties), the use of MOFs as catalyst precursors constitutes a very appealing approach.

2. Results and Discussion

2.1. Synthesis and Characterization of Ru-Loaded UiO-66

Ru-loaded UiO-66 (Ru_xUiO-66, where x is the nominal Ru-to-Zr molar ratio) was prepared following the procedure described in the literature [31], substituting part of the bulk Zr by Ru in the MOF synthesis gel. The materials will be referred to as Ru_{0.03}UiO-66 (0.3 Ru to 9.7 Zr mol ratio) and Ru_{0.10}UiO-66 (1 Ru to 9 Zr mol ratio). After the hydrothermal synthesis at 100 °C, a nanoparticulated (mean size of 590 ± 20 nm) solid was obtained, as revealed by scanning electron microscopy (SEM) (Figure 1a). Powder X-ray diffraction (XRD) (Figure 1b) patterns of the as-synthesized MOFs revealed that the addition of Ru does not affect the structure of the parent UiO-66, as evidenced by the coincidence with the simulated characteristics diffraction peaks. In addition, no diffraction peaks corresponding to Ru species can be observed, though the low Ru loading can explain their absence. On the other hand, the Fourier-transform infrared (FTIR) spectra of the Ru_xUiO-66 nanocomposites (Figure S1) showed peaks for the Zr–O mode and Zr–O–C symmetric stretching, proving that Zr is the coordination center in the organic framework. Ru vibrational peaks were not detected by FTIR, suggesting that Ru is not coordinated to the UiO-66 skeleton [32,34]. Thermo-gravimetric analyses (TGA) (Figure 1c and Figure S4) were conducted in air to evaluate the thermal stability of Ru_xUiO-66 samples. The weight loss at temperatures below 100 °C is attributed to water desorption, and the loss at around 220 °C is attributed to the presence of residual solvent. Meanwhile, decomposition of the framework organic linker (corresponding to a total weight loss of around 65%) took place at 420 °C for Ru_{0.10}UiO-

66, at 510 °C for Ru_{0.03}UiO-66 and 520 °C for UiO-66. This result can be attributed to a weakening of the interaction between the organic linker and Zr⁴⁺ due to the presence of Ru moieties, thus facilitating the decomposition of the hybrid material [32], though a catalytic effect of Ru on the linkers degradation cannot be ruled out. N₂ adsorption-desorption analyses provided very high specific surface areas of 1220 m²·g⁻¹ and 1247 m²·g⁻¹ for Ru_{0.10}UiO-66 and Ru_{0.03}UiO-66, respectively, which are only slightly lower than that of pristine UiO-66 (1380 m²·g⁻¹). This reduction of superficial area for the hybrid materials suggests the presence of Ru clusters inside the porous network without seriously affecting the textural features of the pure UiO-66.

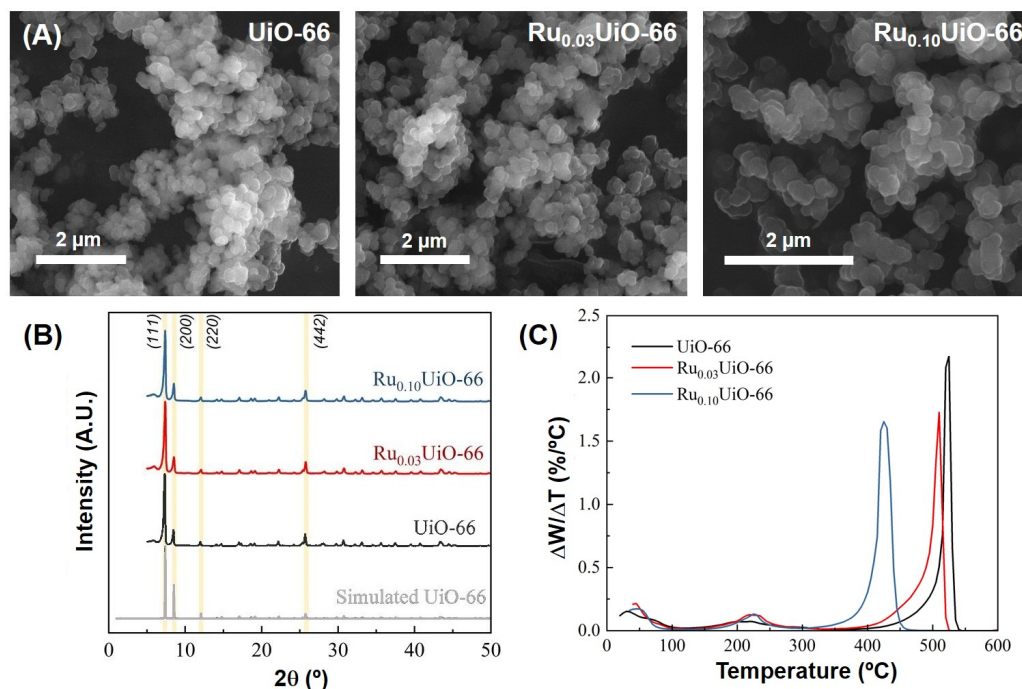


Figure 1. Characterization of Ru_xUiO-66 samples: (A) SEM images, (B) XRD patterns, and (C) Differential TGA curves.

2.2. Preparation and Characterization of MOF-Derived Ru@ZrO₂ Catalysts

500 mg of as-synthesized Ru_xUiO-66 materials were treated under air flow at three different calcination temperatures (400, 500 and 600 °C) to obtain the catalysts. Calcined MOF-derived composites (denoted as Ru@ZrO₂-X, where X indicates the calcination temperature, 400 °C, 500 °C, or 600 °C), were characterized by TEM, XRD, TGA, and N₂ adsorption-desorption. As expected, after calcination, the samples presented a large loss of weight and bulk density due to the elimination of the organic ligand. Their color turned dark; the darker they were, the more Ru in the framework, and they also possessed improved light absorption in the visible range, as evidenced by UV-Vis reflectance spectroscopy (Figure 2c) [35]. Ru content of the materials was determined by inductively coupled plasma atomic emission spectrometry (ICP-AES). The Ru incorporation to the MOF during the synthesis was much lower than expected (0.37 wt.% for the as-synthesized Ru₁₀UiO-66 vs. the nominal value of 5.84 wt.%), resulting in catalysts with very low Ru loads. The ruthenium incorporation could be favored by increasing the synthesis temperature. Results also showed that the calcination treatment caused a slight change in the ruthenium content from 0.34 wt.% in Ru_{0.10}@ZrO₂-400 °C to 0.26 wt.% and 0.24 wt.% for samples Ru_{0.10}@ZrO₂-500 °C and Ru_{0.10}@ZrO₂-600 °C, respectively. In the case of the lowest Ru to Zr molar ratio, the Ru content diminished to 0.04 wt.% for Ru_{0.03}@ZrO₂-600 °C.

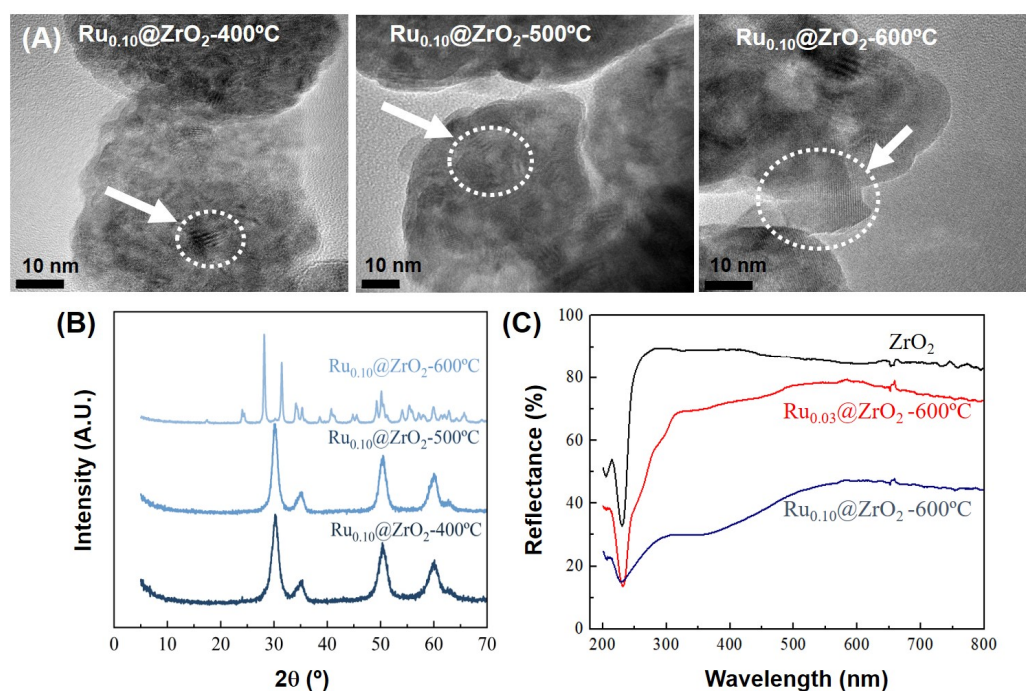


Figure 2. Characterization of the MOF-derived catalysts obtained via controlled calcination at 400, 500, and 600 °C of Ru_xUiO-66 materials. (A) TEM images; (B) XRD patterns of the Ru_{0.10}@ZrO₂ catalysts; and (C) UV-Vis reflectance measurements.

As it can be seen in the TEM images depicted in Figure 2a and Figure S2, polycrystalline nanoparticulated solids were obtained. The crystallinity of the particles (encircled in the images) increased with the calcination temperature. No Ru nanoclusters could be observed in the micrographs, probably due to the low incorporation of Ru and its high dispersion, as confirmed by EDS (Energy Dispersive Spectroscopy) analysis (Figure S2). X-ray patterns in Figure 2b and Figure S3 reveal the presence of monoclinic ZrO₂ in the Ru@ZrO₂-600 °C samples. Meanwhile, Ru@ZrO₂-400 °C and Ru@ZrO₂-500 °C contain cubic ZrO₂ [36–38]. Lippi et al. [31] demonstrated, by operating XRD, the importance of the monoclinic ZrO₂ phase transitions during thermal treatment to stabilize Ru and obtain active CO₂ methanation catalysts. In our case, Ru species could not be detected by XRD, mainly due to the low Ru content of the bulk materials. Although all treated samples exhibited crystallinity, materials calcined at 400 and 500 °C still contained low amounts of organic residue or non-degraded MOF, as observed by TGA (Figure S4) and FTIR (Figure S1), confirming an incomplete removal of the organic linker.

2.3. Catalytic Tests

Firstly, all the UiO-66 MOF-derived catalysts were tested for the CO₂ methanation in a temperature-controlled Harrick HVC-MRA-5 reaction chamber. An amount of 30 mg of the catalysts were deposited on the chamber mesh placing a thermocouple directly in contact with the catalyst sample. Prior to the methanation tests, an in situ reduction pre-treatment with pure H₂ at 150 °C for 3 h was carried out to assure the presence of Ru in the metallic state. A stoichiometric mixture of H₂ and CO₂, according to a 4:1 molar ratio, was fed to the reactor at a space velocity of 10,000 N mL g_{cat.}⁻¹ h⁻¹, after which the temperature was increased at a controlled rate of 3 °C·min⁻¹ from 80 to 300 °C (see Figure 3a). As pointed out before, the temperature of the thermal treatment was crucial to obtain active materials and achieve good CH₄ yields.

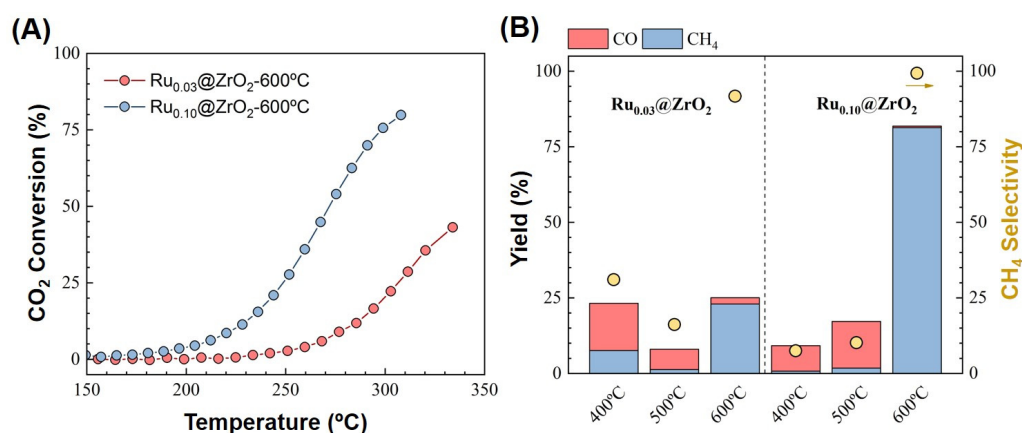


Figure 3. CO₂ methanation performance of MOF-derived materials. (A) Evolution of the CO₂ conversion with the reaction temperature for the catalysts calcined at 600 °C. (B) Effect of the calcination temperature on the reaction yield and selectivity to CH₄ (selected data recorded at 300 °C).

The CH₄ yields and selectivities (see Figure 3b) achieved by the different catalysts demonstrated that the materials treated at 600 °C present excellent methanation performance, meanwhile those treated at lower temperatures exhibit clearly lower activity and higher selectivity to CO. These results can be attributed to the presence of monoclinic ZrO₂ in the catalyst obtained after calcination at 600 °C of the Ru_xUiO-66 precursors, while the samples calcined at lower temperatures contain cubic ZrO₂. It is remarkable that, whereas the Ru_{0.03}@ZrO₂-600 °C shows only improved CH₄ selectivity, Ru_{0.10}@ZrO₂-600 °C exhibits both improved activity and selectivity, thus suggesting a cooperative effect of both Ru and monoclinic ZrO₂. Indeed, Ru_{0.10}@ZrO₂-600 °C catalyst was able to hydrogenate CO₂ to CH₄ with a production rate at 300 °C as high as 65 mmol_{CH₄}·g_{cat.}⁻¹·h⁻¹, CH₄ yield of about 80% and nearly 100% selectivity. The CH₄ production rate achieved with Ru_{0.03}@ZrO₂-600 °C decreased to 20 mmol_{CH₄}·g_{cat.}⁻¹·h⁻¹ due to the low amount of Ru, and the selectivity to methane was 90%. In spite of their comparatively low activity, both Ru_{0.03}@ZrO₂ and Ru_{0.10}@ZrO₂ calcined at 400 °C and 500 °C exhibited high selectivities to CO, similar (low activity and high selectivity to CO) to those achieved with bare ZrO₂ supports for calcined UiO-66 without Ru (Figure S5).

The higher activity and selectivity of the monoclinic ZrO₂ materials obtained after calcination at 600 °C in comparison with their cubic ZrO₂ counterparts reveals a key role of the allotropic form of zirconia on the CO₂ methanation selectivity, indicating that the support is involved in the reaction pathway. Different studies reported in the literature also highlight the importance of the crystalline phase [39], the presence of dopants [40], and the nature of the metallic phase [41] on the CO₂ methanation over Ru/ZrO₂ systems. Ilseemann et al. [42] performed in operando DRIFTS studies with a Ru/ZrO₂ catalysts and found that the formate pathway is predominant at temperatures below 300 °C, at which this species would be formed after C–O bond cleavage of a bidentate carbonate adsorbed on the ZrO₂ surface. These authors also suggested that the formation of formate species is related with the presence of Lewis basic oxygen vacancies that could be a possible reason for the higher activity of monoclinic zirconia.

The most active material, Ru_{0.10}@ZrO₂-600 °C, was selected to carry out the photo-thermal CO₂ hydrogenation (Figure 4). The temperature was increased with the internal heater up to 230 °C, and then, the reaction chamber was illuminated with an ultra-high power visible-range LED. Under an irradiance of 8 Sun, the temperature raised to 250 °C, provoking an increment of the production of CH₄ from 17 mmol_{CH₄}·g_{cat.}⁻¹·h⁻¹ in dark conditions to 23 mmol_{CH₄}·g_{cat.}⁻¹·h⁻¹, which corresponded to an increase in the CO₂ conversion from about 15% to almost 25%. Then, the lamp was switched off for 70 min, and the CH₄ production and temperature values came back to those of the dark conditions.

The procedure was repeated at higher irradiance (24 Sun) that led to a temperature rise up to 310 °C, as well as an increase in the CO₂ conversion up to about 38%. CH₄ production jumped to 32 mmol_{CH₄}·g_{cat.}⁻¹·h⁻¹. Methane selectivity during the whole process was above 99% under dark or illuminated conditions. The conversion enhancement is mainly attributed to the increase in the catalyst temperature, resulting from the absorption of the radiation received. More specific conversion vs. light intensity experiments should be carried out to separately determine both thermal and photocatalytic effects of light as pointed out by Mateo et al. [43,44]. In addition, the temperature increase resulting from light absorption occurs only in the exposed part of the catalytic bed, so a relatively large temperature gradient can be established [45], causing the actual mean temperature, and hence the CO₂ conversion, to be lower than that expected from the whole bed operating isothermally at the temperature read by the thermocouple. Specifically designed catalytic chambers have to be developed for better control of the reaction temperature.

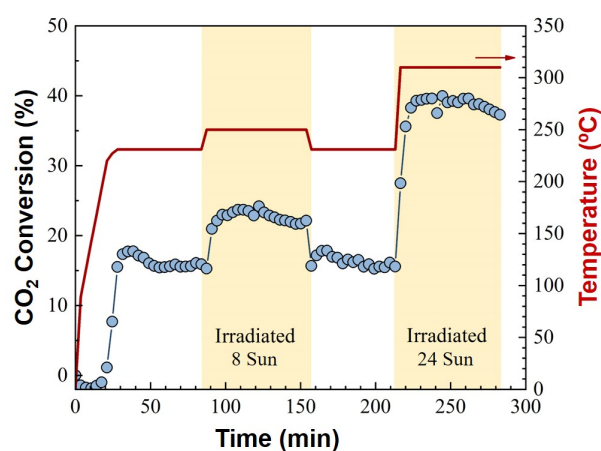


Figure 4. Effect of the visible LED irradiation (8 and 24 Sun) on the photo-thermal hydrogenation of CO₂ with the catalyst Ru_{0.10}@ZrO₂-600 °C.

3. Materials and Methods

3.1. Materials

Terephthalic acid (98%), anhydrous zirconium (IV) chloride (ZrCl₄), ruthenium (III) chloride hydrate (RuCl₃·xH₂O), and hydrochloric acid (HCl, 37%) were supplied by Sigma Aldrich. N,N-dimethylformamide (DMF), ethanol (96%), and methanol were purchased from Scharlab. Calibrated reaction gas mixture 17.9 vol. % CO₂, 71.9 vol. % H₂ and 10.1 vol. % N₂ was provided by Nippon Gases. All reactants were used without further purification.

3.2. MOF Synthesis

Ru-loaded MOF Ru_xUiO-66 (x stands for the nominal Ru/Zr molar ratio) were synthesized following well established procedures for its pristine counterpart UiO-66 (ZrBDC) with a metal to organic ligand molar ratio of 1:2 [30]. Ru was introduced by replacing 3% or 10% of the initial Zr precursor by the Ru salt. A typical synthesis procedure was as follows: for the synthesis of Ru_{0.10}UiO-66, ZrCl₄ (9 mmol) and RuCl₃·xH₂O (1 mmol) were added to a mixture of DMF (60 mL) and 37% HCl (2.4 mL) [31]. Afterwards, H₂BDC (20 mmol) was added to the solution and stirred at room temperature until complete dissolution. The mixture was heated at autogenous pressure at 100 °C for 20 h. The product was recovered by centrifugation and washed with distilled water, ethanol, and methanol. Finally, the Ru-loaded MOF was dried at 70 °C overnight.

3.3. Thermal Treatment

The MOF-derived catalysts were obtained by controlled calcination of the Ru-loaded MOF precursors in a flow-through tubular oven (Hobersal) for 3 h under 20 N mL·min⁻¹

air flow (Nippon Gases, 99.9%). The influence of the temperature of calcination on the catalytic properties of the final product was studied by calcination at 400, 500, and 600 °C. The heating ramp was kept, in all cases, at 10 °C·min⁻¹.

3.4. Characterization Techniques

Scanning electron microscopy (SEM) analyses (CSEM-FEG Inspect) were performed on Ru-loaded MOF precursors to assess crystal morphology and chemical composition. For the MOF-derived oxides, transmission electron microscopy with energy-dispersive X-ray spectroscopy (TEM-EDX) analyses (FEI TECNAI F30) were performed for the same purposes. Purity and crystallinity of both the MOF-precursors and final oxides were evaluated by powder X-ray diffraction (XRD, RIGAKU Ru2500). The XRD patterns were compared to simulated patterns calculated using the software VESTA. Thermal stability of the synthesized compounds was evaluated by differential thermogravimetric analysis (DTGA) over 6 mg of sample with a heating rate of 5 °C·min⁻¹ from room temperature to 700 °C under air flow (TGA/DSC 3+ Mettler Toledo). Textural properties were assessed by N₂ physisorption at 77 K (Micromeritics GEMINI V 2380), and surface area was evaluated applying the Langmuir model. Degree of oxidation after calcination of the MOF precursor was further assessed by Fourier-transform infrared spectroscopy (FTIR) with a high throughput monolithic diamond attenuated total reflectance (ATR) (Jasco FT/IR-4700 Spectrometer), accumulation of 50 scans, resolution of 1 cm⁻¹. Light absorption properties were analyzed with a flame spectrometer (Ocean Optics) in the 200–800 nm range with a UV-visible reflection probe. Finally, the Ru content of the catalysts precursors was analyzed by inductively coupled plasma atomic emission spectroscopy (ICP-AES) (Varian Vista MPX Radial). The digestion of the ruthenium containing materials was carried out following the fusion method reported by T. Suoranta et al. [46].

3.5. Catalytic Tests

The CO₂ hydrogenation tests were carried out in temperature-controlled Harrick HVC-MRA-5 reaction chamber. The reactor temperature was measured by means of a type K thermocouple placed on the catalyst surface [45]. Reaction gases were analyzed with an online gas chromatograph (Agilent 990 Micro GC System provided with a molecular sieve 5A column for permanent gases and PPU column for CO₂ determination). Stoichiometric mixture of H₂ and CO₂ according to a 4:1 molar ratio (17.9 vol. % CO₂, 71.9 vol. % H₂ and 10.1 vol. % of N₂ as internal standard) was fed to the reactor at a space velocity of 10,000 mL g⁻¹ h⁻¹. Prior to any experiments, the Ru-based catalysts (30 mg) were subjected to an in situ reduction pre-treatment with pure H₂ for 2 h at 150 °C. Then, for the direct experiments, the reaction mixture was introduced into the reactor, and the temperature was increased with a rate of 3 °C·min⁻¹ from 80 to 300 °C, and it was kept constant for 50 min at 300 °C.

To evaluate the photo-thermal activity, the most active catalysts were placed into the reactor, and the temperature was increased up to 230 °C and kept at this temperature for 60 min. Subsequently, the catalyst was illuminated with an ultra-high power (30 W) visible-range LED (Figure S6) (LEDM-5500 White HP—Pyroistech S.L.) placed 1 cm above the catalyst surface. Position of the LED-lamp and its luminous flux can be controlled to regulate the irradiance received by the sample. Maximum irradiance received corresponds to 2.4 W·cm⁻² (1 Sun = 0.1 W·cm⁻²). The temperature on the surface of the catalyst was continuously registered during the process.

The CO₂ conversion (X , %), CH₄ selectivity (S_{CH_4} , %), and yield (Y_{CH_4} , %) were calculated as follows:

$$X_{CO_2} = \frac{F_{CO_2} (in) - F_{CO_2} (out)}{F_{CO_2} (in)} \times 100\% \quad (1)$$

$$S_{CH_4} = \frac{F_{CH_4} (out)}{F_{CH_4} (out) + F_{CO} (out)} \times 100\% \quad (2)$$

$$Y_{CH_4} = X_{CO_2} \cdot S_{CH_4} \times 100\% \quad (3)$$

where $F_{CO_2(in)}$ and $F_{CO_2(out)}$ are the molar flows of CO_2 at the reactor inlet and outlet, respectively. Similarly, $F_{CH_4(out)}$ and $F_{CO(out)}$ are the molar flows of CH_4 and CO at the reactor outlet.

4. Conclusions

The use of MOFs as catalyst precursors has resulted in an interesting approach to achieve high metallic dispersion all over the catalyst surface, as well as good control of the support properties. Small quantities of Ru were incorporated during the hydrothermal synthesis of the Zr-based UiO-66 MOF, and subsequently, MOF-derived $Ru@ZrO_2$ catalysts were obtained via controlled calcination. Calcination at 600 °C was crucial to tune the crystalline phase (monoclinic) of ZrO_2 that provided the most outstanding methanation results (in terms of conversion and selectivity). The most active material, $Ru_{0.10}@ZrO_2-600$ °C, with a final amount of Ru around 0.24 wt. %, was tested under high power visible LED illumination. A CO_2 conversion enhancement from 18% to 38% was observed under 24 Sun irradiance as a result of the increase in the catalyst temperature due to the absorption of the radiation received.

Supplementary Materials: The following supporting information can be downloaded at: <https://www.mdpi.com/article/10.3390/chemistry5020051/s1>, Figure S1: FTIR spectra, Figure S2: TEM images and EDX analysis, Figure S3: Simulated XRD for ZrO_2 , Figure S4: TGA curves of $Ru_xUiO-66$ and derived- $Ru_x@ZrO_2$ catalysts, Figure S5: CO_2 methanation performance of MOF-derived ZrO_2 without Ru content, Figure S6: Spectral power distribution of ultra-high power LEDM-5500 White HP—Pyroistech S.L.

Author Contributions: Conceptualization, I.P. and L.M.G.; methodology, M.L., F.A., M.I., and I.P.; investigation and data curation, M.L., F.A., A.E., and M.I.; writing and editing, M.L., F.A., I.P., and L.M.G.; funding acquisition, I.P. and L.M.G. All authors have read and agreed to the published version of the manuscript.

Funding: Financial support was obtained from Spanish Agencia Estatal de Investigación and Spanish Ministerio de Ciencia e Innovación MCIN/AEI/10.13039/501100011033/ and FEDER “Una manera de hacer Europa” (grants PID2019-106687RJ-I00/AEI/ 10.13039/501100011033 and PID2021-127265OB-C21), as well as from Plan de Recuperación, Transformación y Resiliencia and NextGenerationEU (grants PLEC2022-009221 and TED2021-130846B-100), which is gratefully acknowledged. M.L. and M.I. thank Spanish Ministerio de Universidades and Unión Europea-NextGenerationEU for the postdoctoral “Margarita Salas” and FPU 18/01877 grants, respectively. A.E. thanks Universidad Pública de Navarra for the predoctoral fellowship. L.M.G. thanks the Banco de Santander and Universidad Pública de Navarra for their financial support under “Programa de Intensificación de la Investigación 2018” initiative.

Data Availability Statement: The data presented in this study are available on request from the corresponding authors.

Acknowledgments: Authors acknowledge the use of XRD analysis service of Servicio General de Apoyo a la Investigación-SAL, Universidad de Zaragoza and the instrumentation as well as the technical advice provided by the National Facility ELECMI ICTS, node Laboratorio de Microscopias Avanzadas (LMA) at Universidad de Zaragoza.

Conflicts of Interest: The authors declare no conflict of interest.

References

1. Intergovernmental Panel on Climate Change, IPCC. *Climate Change 2014: Mitigation of Climate Change*; Cambridge University Press: Cambridge, UK, 2015; ISBN 9781107058217.
2. Álvarez, A.; Bansode, A.; Urakawa, A.; Bavykina, A.V.; Wezendonk, T.A.; Makkee, M.; Gascon, J.; Kapteijn, F. Challenges in the Greener Production of Formates/Formic Acid, Methanol, and DME by Heterogeneously Catalyzed CO_2 Hydrogenation Processes. *Chem. Rev.* **2017**, *117*, 9804–9838. [[CrossRef](#)] [[PubMed](#)]

3. Goud, D.; Gupta, R.; Maligal-Ganesh, R.; Peter, S.C. Review of Catalyst Design and Mechanistic Studies for the Production of Olefins from Anthropogenic CO₂. *ACS Catal.* **2020**, *10*, 14258–14282. [[CrossRef](#)]
4. Ye, R.P.; Ding, J.; Gong, W.; Argyle, M.D.; Zhong, Q.; Wang, Y.; Russell, C.K.; Xu, Z.; Russell, A.G.; Li, Q.; et al. CO₂ Hydrogenation to High-Value Products via Heterogeneous Catalysis. *Nat. Commun.* **2019**, *10*, 5698. [[CrossRef](#)] [[PubMed](#)]
5. Corma, A.; Garcia, H. Photocatalytic Reduction of CO₂ for Fuel Production: Possibilities and Challenges. *J. Catal.* **2013**, *308*, 168–175. [[CrossRef](#)]
6. Ramirez, A.; Sarathy, S.M.; Gascon, J. CO₂ Derived E-Fuels: Research Trends, Misconceptions, and Future Directions. *Trends Chem.* **2020**, *2*, 785–795. [[CrossRef](#)]
7. Senderens, J.B.; Sabatier, P. Nouvelles Synthèses Du Méthane. *Comptes. Rendus. Acad. Sci.* **1902**, *82*, 514–516.
8. Vogt, C.; Monai, M.; Kramer, G.J.; Weckhuysen, B.M. The Renaissance of the Sabatier Reaction and Its Applications on Earth and in Space. *Nat. Catal.* **2019**, *2*, 188–197. [[CrossRef](#)]
9. Zhang, F.; Li, Y.H.; Qi, M.Y.; Yamada, Y.M.A.; Anpo, M.; Tang, Z.R.; Xu, Y.J. Photothermal Catalytic CO₂ Reduction over Nanomaterials. *Chem. Catal.* **2021**, *1*, 272–297. [[CrossRef](#)]
10. Song, C.; Wang, Z.; Yin, Z.; Xiao, D.; Ma, D. Principles and Applications of Photothermal Catalysis. *Chem. Catal.* **2022**, *2*, 52–83. [[CrossRef](#)]
11. Meng, X.; Wang, T.; Liu, L.; Ouyang, S.; Li, P.; Hu, H.; Kako, T.; Iwai, H.; Tanaka, A.; Ye, J. Photothermal Conversion of CO₂ into CH₄ with H₂ over Group VIII Nanocatalysts: An Alternative Approach for Solar Fuel Production. *Angew. Chem.* **2014**, *126*, 11662–11666. [[CrossRef](#)]
12. Ghossoub, M.; Xia, M.; Duchesne, P.N.; Segal, D.; Ozin, G. Principles of Photothermal Gas-Phase Heterogeneous CO₂ Catalysis. *Energy Environ. Sci.* **2019**, *12*, 1122–1142. [[CrossRef](#)]
13. Fang, S.; Hu, Y.H. Thermo-Photo Catalysis: A Whole Greater than the Sum of Its Parts. *Chem. Soc. Rev.* **2022**, *51*, 3609–3647. [[CrossRef](#)] [[PubMed](#)]
14. Lv, C.; Bai, X.; Ning, S.; Song, C.; Guan, Q.; Liu, B.; Li, Y.; Ye, J. Nanostructured Materials for Photothermal Carbon Dioxide Hydrogenation: Regulating Solar Utilization and Catalytic Performance. *ACS Nano* **2022**, *17*, 1725–1738. [[CrossRef](#)] [[PubMed](#)]
15. Li, Z.; Shi, R.; Zhao, J.; Zhang, T. Ni-Based Catalysts Derived from Layered-Double-Hydroxide Nanosheets for Efficient Photothermal CO₂ Reduction under Flow-Type System. *Nano Res.* **2021**, *14*, 4828–4832. [[CrossRef](#)]
16. Li, X.; Yu, J.; Jaroniec, M.; Chen, X. Cocatalysts for Selective Photoreduction of CO₂ into Solar Fuels. *Chem. Rev.* **2019**, *119*, 3962–4179. [[CrossRef](#)]
17. Li, Y.; Liu, Z.; Rao, Z.; Yu, F.; Bao, W.; Tang, Y.; Zhao, H.; Zhang, J.; Wang, Z.; Li, J.; et al. Experimental and Theoretical Insights into an Enhanced CO₂ Methanation Mechanism over a Ru-Based Catalyst. *Appl. Catal. B Environ.* **2022**, *319*, 121903. [[CrossRef](#)]
18. Ullah, S.; Lovell, E.C.; Wong, R.J.; Tan, T.H.; Scott, J.; Amal, R. Light-Enhanced CO₂ Reduction to CH₄ Using Nonprecious Transition-Metal Catalysts. *ACS Sustain. Chem. Eng.* **2020**, *8*, 5056–5066. [[CrossRef](#)]
19. Ulmer, U.; Dingle, T.; Duchesne, P.N.; Morris, R.H.; Tavasoli, A.; Wood, T.; Ozin, G.A. Fundamentals and Applications of Photocatalytic CO₂ Methanation. *Nat. Commun.* **2019**, *10*, 3169. [[CrossRef](#)]
20. Kho, E.T.; Jantarang, S.; Zheng, Z.; Scott, J.; Amal, R. Harnessing the Beneficial Attributes of Ceria and Titania in a Mixed-Oxide Support for Nickel-Catalyzed Photothermal CO₂ Methanation. *Engineering* **2017**, *3*, 393–401. [[CrossRef](#)]
21. Albero, J.; Garcia, H.; Corma, A. Temperature Dependence of Solar Light Assisted CO₂ Reduction on Ni Based Photocatalyst. *Top. Catal.* **2016**, *59*, 787–791. [[CrossRef](#)]
22. González-Rangulan, V.V.; Reyero, I.; Bimbela, F.; Romero-Sarria, F.; Daturi, M.; Gandía, L.M. CO₂ Methanation over Nickel Catalysts: Support Effects Investigated through Specific Activity and Operando IR Spectroscopy Measurements. *Catalysts* **2023**, *13*, 448. [[CrossRef](#)]
23. Zhang, Y.; Xu, J.; Zhou, J.; Wang, L. Metal-Organic Framework-Derived Multifunctional Photocatalysts. *Chin. J. Catal.* **2022**, *43*, 971–1000. [[CrossRef](#)]
24. Oar-Arteta, L.; Wezendonk, T.; Sun, X.; Kapteijn, F.; Gascon, J. Metal Organic Frameworks as Precursors for the Manufacture of Advanced Catalytic Materials. *Mater. Chem. Front.* **2017**, *1*, 1709–1745. [[CrossRef](#)]
25. Khan, I.S.; Garzon-Tovar, L.; Mateo, D.; Gascon, J. Metal-Organic-Frameworks and Their Derived Materials in Photo-Thermal Catalysis. *Eur. J. Inorg. Chem.* **2022**, *2022*, e202200316. [[CrossRef](#)]
26. Khan, I.S.; Mateo, D.; Shterk, G.; Shoinchorova, T.; Poloneeva, D.; Garzón-Tovar, L.; Gascon, J. An Efficient Metal–Organic Framework-Derived Nickel Catalyst for the Light Driven Methanation of CO₂. *Angew. Chem. Int. Ed.* **2021**, *60*, 26476–26482. [[CrossRef](#)]
27. Gong, X.; Wang, W.W.; Fu, X.P.; Wei, S.; Yu, W.Z.; Liu, B.; Jia, C.J.; Zhang, J. Metal-Organic-Framework Derived Controllable Synthesis of Mesoporous Copper-Cerium Oxide Composite Catalysts for the Preferential Oxidation of Carbon Monoxide. *Fuel* **2018**, *229*, 217–226. [[CrossRef](#)]
28. Zheng, L.; Li, X.; Du, W.; Shi, D.; Ning, W.; Lu, X.; Hou, Z. Metal-Organic Framework Derived Cu/ZnO Catalysts for Continuous Hydrogenolysis of Glycerol. *Appl. Catal. B Environ.* **2017**, *203*, 146–153. [[CrossRef](#)]
29. Zeng, L.; Wang, Y.; Li, Z.; Song, Y.; Zhang, J.; Wang, J.; He, X.; Wang, C.; Lin, W. Highly Dispersed Ni Catalyst on Metal-Organic Framework-Derived Porous Hydrous Zirconia for CO₂ Methanation. *ACS Appl. Mater. Interfaces* **2020**, *12*, 17436–17442. [[CrossRef](#)]
30. Shearer, G.C.; Chavan, S.; Ethiraj, J.; Vitillo, J.G.; Svelle, S.; Olsbye, U.; Lamberti, C.; Bordiga, S.; Lillerud, K.P. Tuned to Perfection: Ironing out the Defects in Metal-Organic Framework UiO-66. *Chem. Mater.* **2014**, *26*, 4068–4071. [[CrossRef](#)]

31. Lippi, R.; D'Angelo, A.M.; Li, C.; Howard, S.C.; Madsen, I.C.; Wilson, K.; Lee, A.F.; Sumbly, C.J.; Doonan, C.J.; Patel, J.; et al. Unveiling the Structural Transitions during Activation of a CO₂ Methanation Catalyst Ru₀/ZrO₂ Synthesised from a MOF Precursor. *Catal. Today* **2021**, *368*, 66–77. [[CrossRef](#)]
32. Xu, W.; Dong, M.; Di, L.; Zhang, X. A Facile Method for Preparing UiO-66 Encapsulated Ru Catalyst and Its Application in Plasma-Assisted CO₂ Methanation. *Nanomaterials* **2019**, *9*, 1432. [[CrossRef](#)]
33. Fereja, S.L.; Zhang, Z.; Fang, Z.; Guo, J.; Zhang, X.; Liu, K.; Li, Z.; Chen, W. High-Entropy Oxide Derived from Metal-Organic Framework as a Bifunctional Electrocatalyst for Efficient Urea Oxidation and Oxygen Evolution Reactions. *ACS Appl. Mater. Interfaces* **2022**, *14*, 38727–38738. [[CrossRef](#)] [[PubMed](#)]
34. Pourkhosravani, M.; Dehghanpour, S.; Farzaneh, F. Palladium Nanoparticles Supported on Zirconium Metal Organic Framework as an Efficient Heterogeneous Catalyst for the Suzuki-Miyaura Coupling Reaction. *Catal. Lett.* **2016**, *146*, 499–508. [[CrossRef](#)]
35. Akilandeswari, S.; Rajesh, G.; Govindarajan, D.; Thirumalai, K.; Swaminathan, M. Efficacy of Photoluminescence and Photocatalytic Properties of Mn Doped ZrO₂ Nanoparticles by Facile Precipitation Method. *J. Mater. Sci. Mater. Electron.* **2018**, *29*, 18258–18270. [[CrossRef](#)]
36. Han, Y.; Zhu, J. Surface Science Studies on the Zirconia-Based Model Catalysts. *Top. Catal.* **2013**, *56*, 1525–1541. [[CrossRef](#)]
37. Sadati, S.M.; Feghhi, S.A.H.; Mohammadi, K. Effect of Time Exposure on Themoluminescend Glow Curve For UV-Induced ZrO₂:Mg Phosphor. *Radiat. Prot. Dosim.* **2017**, *173*, 333–337.
38. Prakashbabu, D.; Hari Krishna, R.; Nagabhushana, B.M.; Nagabhushana, H.; Shivakumara, C.; Chakradar, R.P.S.; Ramalingam, H.B.; Sharma, S.C.; Chandramohan, R. Low Temperature Synthesis of Pure Cubic ZrO₂ Nanopowder: Structural and Luminescence Studies. *Spectrochim. Acta Part A Mol. Biomol. Spectrosc.* **2014**, *122*, 216–222. [[CrossRef](#)]
39. Nagase, H.; Naito, R.; Tada, S.; Kikuchi, R.; Fujiwara, K.; Nishijima, M.; Honma, T. Ru Nanoparticles Supported on Amorphous ZrO₂ for CO₂ Methanation. *Catal. Sci. Technol.* **2020**, *10*, 4522–4531. [[CrossRef](#)]
40. Gao, M.; Zhang, J.; Zhu, P.; Liu, X.; Zheng, Z. Unveiling the Origin of Alkali Metal Promotion in CO₂ Methanation over Ru/ZrO₂. *Appl. Catal. B Environ.* **2022**, *314*, 121476. [[CrossRef](#)]
41. Alves, L.M.N.C.; Almeida, M.P.; Ayala, M.; Watson, C.D.; Jacobs, G.; Rabelo-Neto, R.C.; Noronha, F.B.; Mattos, L.V. CO₂ Methanation over Metal Catalysts Supported on ZrO₂: Effect of the Nature of the Metallic Phase on Catalytic Performance. *Chem. Eng. Sci.* **2021**, *239*, 116604. [[CrossRef](#)]
42. Ilsemann, J.; Murshed, M.M.; Gesing, T.M.; Kopyscinski, J.; Bäumer, M. On the Support Dependency of the CO₂ Methanation—Decoupling Size and Support Effects. *Catal. Sci. Technol.* **2021**, *11*, 4098–4114. [[CrossRef](#)]
43. Mateo, D.; Cerrillo, J.L.; Durini, S.; Gascon, J. Fundamentals and Applications of Photo-Thermal Catalysis. *Chem. Soc. Rev.* **2021**, *50*, 2173–2210. [[CrossRef](#)]
44. Mateo, D.; Maity, P.; Shterk, G.; Mohammed, O.F.; Gascon, J. Tunable Selectivity in CO₂ Photo-Thermal Reduction by Perovskite-Supported Pd Nanoparticles. *ChemSusChem* **2021**, *14*, 5525–5533. [[CrossRef](#)] [[PubMed](#)]
45. Li, X.; Liu, J.; Everitt, H.O. Untangling Thermal and Nonthermal Effects in Plasmonic Photocatalysis. In *Plasmonic Catalysis: From Fundamentals to Applications*; John Wiley & Sons, Ltd.: Hoboken, NJ, USA, 2021; pp. 191–230. ISBN 9783527347506.
46. Suoranta, T.; Niemelä, M.; Perämäki, P. Comparison of Digestion Methods for the Determination of Ruthenium in Catalyst Materials. *Talanta* **2014**, *119*, 425–429. [[CrossRef](#)] [[PubMed](#)]

Disclaimer/Publisher's Note: The statements, opinions and data contained in all publications are solely those of the individual author(s) and contributor(s) and not of MDPI and/or the editor(s). MDPI and/or the editor(s) disclaim responsibility for any injury to people or property resulting from any ideas, methods, instructions or products referred to in the content.